EDGE ARTICLE

Exploring the molecular design principles for efficient diarylethene photoacid and photohydride generators based on the photochemical reaction mechanism†

Yifan Su,[ab] Dexin Zheng,[ab] Lingfeng Ge,[ab] Le Yu,*[c] David Lee Phillips,[d] Jiani Ma [iD] *[ab] and Yu Fang [iD] [ab]

Photoacid generators (PAGs) and photohydride generators (PHGs) are specific photolabile protecting groups that release acid and hydride, respectively. Over the past decade, great efforts have been devoted to developing novel PAGs and PHGs with advanced efficiency, among which, two of the promising candidates are diarylethene (DAE)-based PAGs and PHGs, which release acids/hydrides during photochromic electrocyclization. The release quantum yield for PAGs is acceptable, while that of PHGs is only 4.2% even after molecular structure modification. In this work, time-resolved transient absorption spectroscopies with femtosecond and nanosecond resolutions along with DFT/TD-DFT calculations were utilized to unravel the detailed photochemical reaction mechanisms of DAE-based PAGs (**1o**) and PHGs (**2o**), respectively. The results show that the different photochemical mechanisms are the key that leads to distinctive release quantum yields between **1o** and **2o**. The factors affecting the release quantum yield are discussed in detail, and several key design principles are proposed to facilitate future rational design of DAE-based PAGs and PHGs.

Introduction

Photolabile protecting groups (PPGs) are currently widely used for photocontrolled chemical and biological processes[1–7] for their excellent spatial and kinetic control over the release of caged molecules.[8–10] Different leaving groups can be connected to PPGs with specific functions, such as photoCORMs (photo-activatable CO-releasing moieties), photoNORMs (photo-activatable nitric oxide-releasing moieties), and photoactivatable H$_2$S-releasing molecules, as well as photoacid generators (PAGs)[11–14] and photohydride generators (PHGs).[15]

PAGs generate acids upon light irradiation and have potential applications in polymer science and biomedicine.[16,17] Zhang designed and synthesized BODIPY-based PAGs with visible light

[a]Key Laboratory of Applied Surface and Colloid Chemistry, Ministry of Education, School of Chemistry and Chemical Engineering, Shaanxi Normal University, Xi'an 710119, China. E-mail: majiani@snnu.edu.cn

[b]Institute of New Concept Sensors and Molecular Materials, Shaanxi Normal University, Xi'an 710119, China

[c]Key Laboratory of Synthetic and Natural Functional Molecule Chemistry of Ministry of Education, College of Chemistry and Materials Science, Northwest University, Xi'an 710127, China. E-mail: yule@nwu.edu.cn

[d]Department of Chemistry, The University of Hong Kong, Pokfulam Road, Hong Kong SAR, P. R. China

† Electronic supplementary information (ESI) available. See DOI: https://doi.org/10.1039/d4sc06202g

activation.[18] Fagnoni reported visible-light-driven arylazo sulfone-based PAGs, whose acid release could be tuned by changing the media: a weak acid (sulfinic acid) in nitrogen-purged solutions and a strong acid (sulfonic acid) in oxygen-purged solutions.[19] Liao's group investigated merocyanine-based PAGs, which underwent visible-light induced *trans–cis* isomerization, followed by proton dissociation, and finally underwent a nucleophilic ring closing reaction, which achieves nearly complete proton dissociation and can alter the pH value of the solution.[20] Komogortsev *et al.* reported tosylated derivatives of terarylenes which could serve as UV-induced PAGs with the photoreaction yield exceeding 90%. However, their photo-generation rates were low and a complete transformation required more than 16 hours.[21] PHGs refer to molecules that release a hydrogen anion (hydride) upon irradiation,[22] and they can be used for photochemical reduction of CO$_2$.[23] Glusac's group studied the hydride release mechanism of 10-methyl-9-phenyl-9,10-dihydroacridine and proposed a stepwise electron/hydrogen-atom transfer mechanism.[24]

DAE derivatives have been used as light-sensitive molecules, and their light-triggered 6π-electrocyclization processes have been studied extensively.[25–37] DAE transforms from its initial open-form (o) to a closed-form (c) after photocyclization. Shirinian found that the photochemical transformations of DAEs containing a five-membered heterocyclic ring and phenyl moiety went through tandem photocyclization/[1,9]-
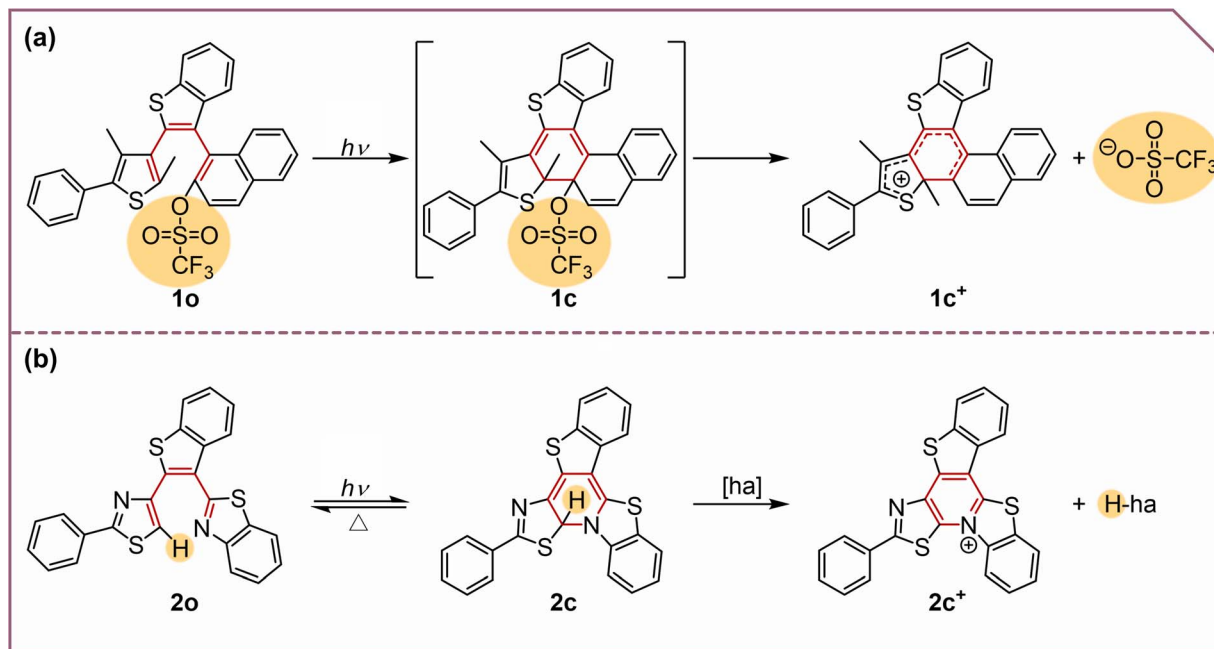
Scheme 1 Photochemical reactions of (a) 1o and (b) 2o. "ha" refers to the "hydride acceptor".

sigmatropic rearrangement/heterocyclic ring opening processes.[38] They also found that *ortho*-bromine-substituted DAEs upon UV irradiation lead to bicyclic fused aromatics in tetrahydrofuran (THF), and could release a bromide cation (Lewis acid), which could catalyze electrophilic reactions.[39] The Nakashima group and the Kawai group developed a series of PAGs based on DAEs. They first designed self-contained proton releasing PAGs that could quantitatively offer Brønsted acids such as MeOH and MeSO₃H[40] and later developed one that released CF₃SO₃H, a super acid.[41] They later developed a similar molecule (denoted as 1o, see Scheme 1a) which released a triflate anion with quantum yields up to 50% upon UV irradiation and also generated a carbocation that can act as a Lewis acid.[14] When the naphthalene connected to the leaving base group in the DAE-based PAG is replaced by benzothiazole, the molecule may release a hydride ion by forming a new C–N bond. These two research groups designed a benzothiazole-containing ter-arylene framework as a PHG (denoted as 2o, see Scheme 1b).[42] Unfortunately, the release quantum yield is only 4.2%.[22] Great efforts have been devoted to improving the efficiency by modifying the three heterocycles, but no significant progress has been made until now.

To facilitate the rational design of DAE-based PAGs and PHGs, 1o and 2o were selected as the model compounds of PAGs and PHGs, respectively, for our reaction mechanism study using femtosecond and nanosecond transient absorption (fs-TA and ns-TA) spectroscopy. Excited-state TD-DFT calculations are performed to help analyze the experimental spectra and draw potential energy curves (PECs). With the detailed and explicit reaction mechanisms in hand, key designing principles of efficient PHGs are concluded.

Results and discussion

Both 1o and 2o share the same DAE skeleton as well as a benzothiazole unit, but also have some specific chemical structures that enable them to engage in different photochemical activities, leading to the remarkable different releasing quantum yields.

Photochemical reaction mechanism of PAGs (1o)

The steady-state UV-vis spectrum of 1o was recorded (Fig. S5†) after irradiation for a certain time to monitor the overall photochemical reaction. The result is consistent with that reported by Kawai[14] where the formed species is assigned to 1c⁺. The UV-vis spectrum for 1c⁺ was simulated by employing the M062X functional and 6-311G** basis set, and the good correlation between the experimental spectrum and the calculated one (Fig. S5c†) suggested that the calculation method is appropriate for the molecular system and will be accepted in this work.

For the fs-TA data of 1o in acetonitrile (ACN), the singlet excited state of 1o was observed at an early stage (Fig. 1a). The structures of the singlet excited state of both the parallel (P) conformer (denoted as 1o-P(S₁)) and the antiparallel (AP) conformer (denoted as 1o-AP(S₁)) are shown in Fig. S6.† TD-DFT calculations suggested that both 1o-P(S₁) and 1o-AP(S₁) exist and contribute to the experimental TA spectrum (Fig. 1e). Later, 1o-AP(S₁) decays and 1o-P(S₁) blue-shifted from 406 nm to 400 nm, coupled with isosbestic points at 362 and 415 nm (Fig. 1b). Based on the photolysis experiment by observing 1c⁺, the signals at 340 and 400 nm were assigned to 1c and supported by TD-DFT calculations (Fig. 1f). Subsequently, 1c decreased
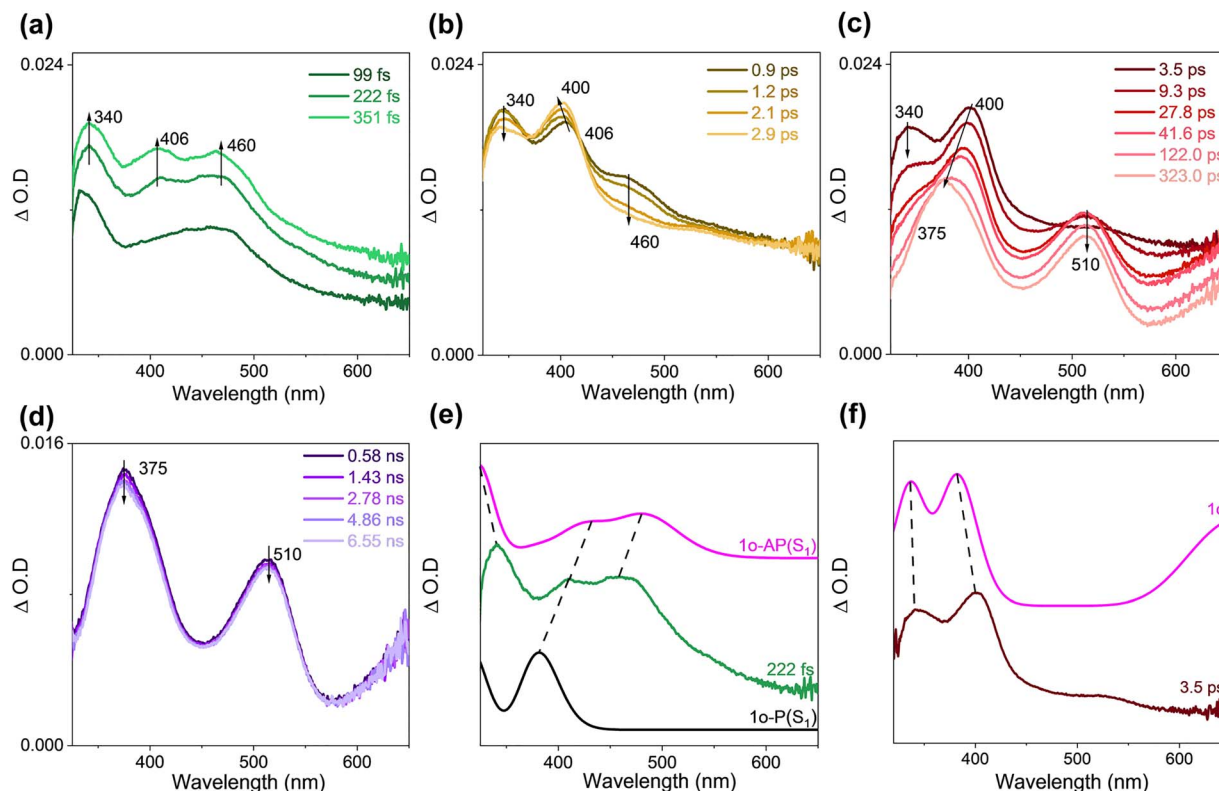
Fig. 1 (a–d) fs-TA spectra of **1o** in ACN (λ_{ex} = 266 nm). (e) The comparison of the computed electronic absorption spectrum of (magenta line) **1o-AP(S$_1$)** and (black line) **1o-P(S$_1$)** with (green line) the fs-TA spectrum recorded at 222 fs. (f) The comparison of (magenta line) the computed electronic absorption spectrum of **1c** with (brown line) the fs-TA spectrum recorded at 3.5 ps. [TD-M062X/6-311G**/SMD (ACN) with a scale factor of 1.02 and a half-width of 1500 cm^{-1}].

accompanying with the generation of new signals at 375 and 510 nm and a broad band absorbing above 600 nm (Fig. 1c).

ns-TA spectra were collected for **1o** under analogous experimental conditions, and the same signals were obtained as seen in the late fs-TA stage (Fig. 2a). These signals were quenched under oxygen quenching conditions, where the decay time constant at 510 nm was 631 ns under open air and 290 ns under

Ar-saturated conditions, respectively (Fig. 2b). Simulated UV-vis spectra of the triplet states of **1o-P** and **1o-AP** (denoted as **1o-P(T$_1$)** and **1o-AP(T$_1$)**, respectively) exhibited reasonable similarity with the ns-TA spectrum (Fig. 2c). Thereafter, the species probed from hundreds of ps to 1.1 μs can be attributed to **1o-P(T$_1$)** and **1o-AP(T$_1$)**.
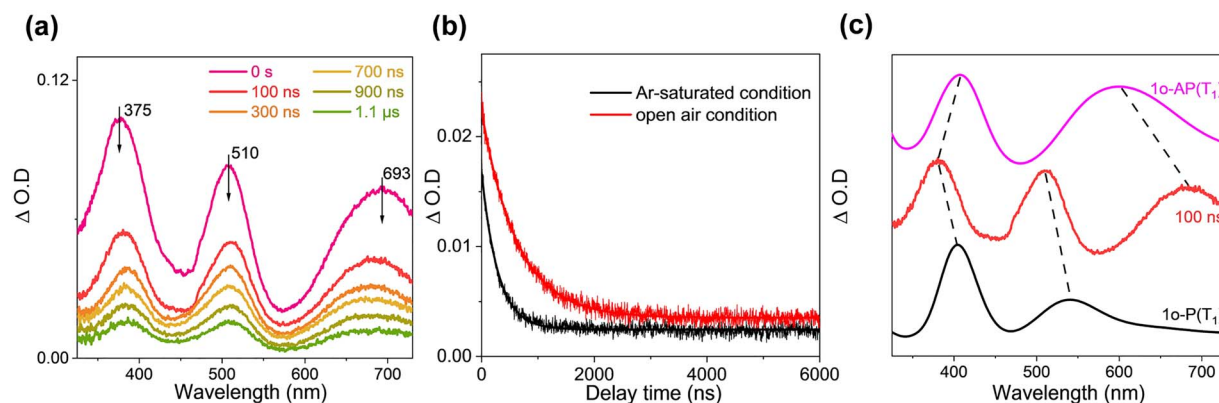
Fig. 2 (a) ns-TA spectra of **1o** in ACN (λ_{ex} = 266 nm). (b) The kinetics and the fitting plots are shown at 510 nm under open air and Ar-saturated conditions in ACN. (c) Comparison of the computed electronic absorption spectrum of (magenta line) **1o-AP(T$_1$)** and (black line) **1o-P(T$_1$)** in ACN with (red line) the ns-TA spectrum recorded at 100 ns. [TD-M062X/6-311G**/SMD (ACN) with a scale factor of 1.02 and a half-width of 1500 cm^{-1}].

Fig. 3 The calculated singlet and triplet state energy level diagram for (a) **1o-AP(S$_0$)** and (b) **1o-P(S$_1$)**. Inset: PEC of **1o-AP**: blue line for the S$_0$ state, red line for the S$_1$ state, and the green dotted line represents the path of the photochemical reaction (energy in kcal mol^{-1}) (the ground state energy of **1o-AP(S$_0$)** is used as zero for obtaining relative energies). [(TD)M062X/6-311G**/SMD (ACN)].

Combining the experimental and DFT/TD-DFT results, it is concluded that **1o-P** and **1o-AP** undergo different pathways. The structures of **1o-P(S$_0$)** and **1o-AP(S$_0$)** are shown in the ESI as Fig. S6.† As shown in the schematic energy diagram (Fig. 3a), after **1o-AP(S$_0$)** is excited to the Franck–Condon (FC) region of the S$_1$ state (denoted as **1o-AP-FC(S$_1$)**), it converts to the semi-ring-closed S$_1$ intermediate, denoted as **1o-AP-CI(S$_1$)**, following an antisymmetrical twisting pathway. At this point, the energies of S$_0$ (62.0 kcal mol^{-1}) and S$_1$ (63.3 kcal mol^{-1}) are quasi-degenerated, indicating the presence of a nearby conical intersection (CI). According to the barrierless PEC connecting **1o-AP-FC(S$_1$)** and **1o-AP-CI(S$_1$)** obtained by a relaxed scan towards the C$_{12}$–C$_{31}$ bond distance within **1o**, the relaxation process on the S$_1$ state could be accomplished at an ultrafast timescale (Fig. S7†). After internal conversion (IC) to the S$_0$ state, **1o-AP-CI(S$_0$)** undergoes a synergistic ring-closing and triflate anion departure process, generating **1c$^+$** and releasing 58.8 kcal mol^{-1} energy. At **1o-AP-FC(S$_1$)**, the energy difference between S$_1$ and T$_4$ states is only 3.5 kcal mol^{-1} with spin orbit coupling matrix elements (SOCME) of 4.5 cm^{-1}, indicating the presence of the feasible intersystem crossing (ISC) pathway. However, the ISC process is a minor pathway as it cannot compete with the IC pathway that follows a steep descending PEC. On the other hand, **1o-P(S$_0$)** is excited to **1o-P-FC(S$_1$)** upon irradiation and quickly evolves to the nearby S$_1$ state minimum (denoted as **1o-P(S$_1$)**), which subsequently switches to the triplet state *via* ISC. Among the possible ISC pathways, S$_1$ → T$_3$ might be the most efficient one for the small energy gap (3.2 kcal mol^{-1}) and large SOCME (4.0 cm^{-1}). Additionally, due to the repulsion between the thiophene and naphthalene moieties, **1o-P** could not convert to the ring-closed form and is therefore a non-reactive conformer. Additionally, the Gibbs free energy of **1o-AP(S$_0$)** is 2.3 kcal mol^{-1} lower than that of **1o-P(S$_0$)** (Table S1†), and thus the **1o-AP(S$_0$)** would have 95% population according to Boltzmann distribution at room temperature. The conversion barrier of **1o-AP(S$_0$)** to **1o-P(S$_0$)** is 3.0 kcal mol^{-1} (Fig. S8†). The stable presence of **1o-AP** is one of the reasons for the high triflate anion release yield.

Photochemical reaction mechanism of PHGs (2o)

The fs-TA and ns-TA results of **2o** in THF are displayed in Fig. S9a–d.† The signal of 550 nm was seen upon irradiation and gradually decreased, and then two bands emerged at 385 and 412 nm, with an isosbestic point at 490 nm. Therefore, the attenuation signal at 550 nm is attributed to the FC state of the AP configuration (the structure is shown in Fig. 5a). The electronic absorption spectra of the singlet excited states of **2o-P** and **2o-AP** (denoted as **2o-P(S$_1$)** and **2o-AP(S$_1$)**, respectively) are simulated (Fig. S9e†) and help to make the assignment of 385 nm to **2o-AP(S$_1$)** and 412 nm to **2o-P(S$_1$)**. The two intermediates then decayed, and the absorbances at 420 and 500 nm appeared. The simulated UV-vis spectra of the triplet **2o-AP** (denoted as **2o-AP(T$_1$)**) and **2c** are in good agreement with the experimental results (Fig. S9f†). The signal at 380 nm can be recognized more obviously in the late ns-TA stage, which is attributed to the triplet **2o-P** (denoted as **2o-P(T$_1$)**) (Fig. S10†).

The fs-TA and ns-TA spectra were collected for **2o** with the addition of methylene blue as a hydride acceptor (Fig. 4a–e). Compared to the situation without methylene blue, the remarkable difference was that a band at 393 nm was produced after 10 μs in ns-TA spectra (Fig. 4e). Methylene blue stabilizes the hydride ion and therefore facilitates the generation of the oxidation product **2c$^+$**. The comparison between the experimental spectrum at 15 μs and the calculated electronic absorption spectrum confirms the signal at 393 nm to be **2c$^+$** (Fig. 4f). The TA data of **2o** in THF with addition of NH$_4$PF$_6$ (Fig. S11†) unravelled that **2c$^+$** decreased in the late stage of ns-TA. This is explained by the fact that the added NH$_4$PF$_6$ can react with the oxidation products to form ion pairs (Fig. S12†).

The molecule **2o** is composed of three groups, the phenyl-thiazole (PT) and benzothiazole (BTZ) groups are linked to the central benzothiophene (BTP) *via* a single bond, and the free-standing or synergistic twisting of PT and BTZ gives rise to various **2o-AP** and **2o-P** conformers. Only one enantiomer within each chiral pair is discussed (the relative energy, Gibbs free energy and thermal weight of all enantiomers are listed in

Fig. 4 (a–c) fs-TA spectra and (d and e) ns-TA spectra of **2o** in THF with addition of methylene blue (λ_{ex} = 355 nm). (f) Comparison of (green line) the computed electronic absorption spectrum of **2c$^+$** with (purple line) the ns-TA spectrum recorded at 15 μs. [TD-M062X/6-311G**/SMD (THF) with a scale factor of 1.02 and a half-width of 1500 cm^{-1}].

Table S2†), including two AP conformers (**2o-AP$_a$(S$_0$)** and **2o-AP$_b$(S$_0$)**) and three P conformers (**2o-P$_a$(S$_0$)**, **2o-P$_b$(S$_0$)** and **2o-P$_c$(S$_0$)**). Different from **1o**, the AP conformers of **2o** are a minority (25% population in total), while, among the majority non-reactive **2o-P** conformers, **2o-P$_a$(S$_0$)** is the most stable one. The energy (free energy) difference between **2o-AP$_a$(S$_0$)** and **2o-AP$_b$(S$_0$)** is only 0.0(4) (0.6) kcal mol^{-1} (Table S2†), and they could interconvert *via* a barrier of 4.7 kcal mol^{-1} (Fig. 5). According to the ground state relaxed scan PEC along the C$_{22}$–N$_{11}$ distance (r_{C-N}) in Fig. S13,† **2o-AP$_b$(S$_0$)** could accomplish the cyclization process by overcoming a 30.7 kcal mol^{-1} barrier (**2o-TS(S$_0$)**) and yield the hydrogenated intermediate **2c(S$_0$)** (Fig. 5a). The ring-closing reaction of **2o** could also take place upon photoexcitation (PEC given in Fig. S14†): **2o-FC$_a$(S$_1$)** and **2o-FC$_b$(S$_1$)** quickly evolve into the stable S$_1$ state intermediate **2o(S$_1$)** (r_{C-N} = 1.8 Å) *via* synergistic twisting of PT and BTZ. Along the S$_1$ ring-closing pathway, **2o(S$_1$)** could sequentially evolve as **2o-CI(S$_1$)** (r_{C-N} = 1.7 Å) and **2c(S$_1$)** (r_{C-N} = 1.4 Å) by absorbing energies of 1.7 and 2.4 kcal mol^{-1}. If IC takes place at the CI region, **2o-CI(S$_1$)** would convert to **2c(S$_0$)** immediately. The entire reaction process of **2o** follows a ring-closing pathway on both S$_1$ and S$_0$ states. Since **2c** is a stable intermediate, the dehydrogenation process can only occur with assistance of a hydride acceptor to generate **2c$^+$**, implying a stepwise route for the photoinduced dehydrogenation of **2o**. The triplet ring-closing pathway of **2o** is negligible. At **2o(S$_1$)**, the only possible ISC channel is S$_1$ → T$_1$ with an energy gap of 4.8 kcal mol^{-1}, where the ISC rate would be inefficient due to rather small SOCME (0.5 cm^{-1}). Even the ISC takes place, the intermediate could transform into **2o(T$_1$)** (36.7 kcal mol^{-1}) or **2c(T$_1$)** (25.9 kcal mol^{-1}), which was located at each end of the

triplet ring-closing pathway of **2o**. Alternatively, when the three nonreactive **2o-P(S$_0$)** conformers are excited to the S$_1$ state, the dominant relaxation pathway for all of them is S$_1$ → T$_2$ ISC as shown in Fig. 5b. The involvement of triplet states in photo-relaxation of **2o** is in agreement with TA experimental studies by detecting **2o-P(T$_1$)** (Fig. S9d and S10†).

Inspired by the distinguished photoreleasing efficiency of **1o**, we propose the following ideas to improve the quantum yield of **2o** based on the above mentioned experimental and theoretical results. First, compared with thermo-dynamically favorable **1o-AP(S$_0$)**, **2o-AP(S$_0$)** is minority among all **2o** conformers at room temperature. To stabilize **2o-AP(S$_0$)** and increase its thermal population, enhancing the rigidity of the skeleton is a possible strategy, *e.g.* inhibiting the rotation of PT and BTZ groups *via* a single bond by introducing steric hindrance or an intramolecular hydrogen bond. Second, as screened by steady-state UV-vis experiments, **1c** releases a tri-flate anion and then spontaneously generates **1c$^+$**, while **2c$^+$** can only be observed in the presence of a hydride acceptor. As well, the energy barrier for the reverse ring-opening process of **2c** (15.5 kcal mol^{-1}) is much lower than that of **1c$^+$** (58.8 kcal mol^{-1}). Thus, the **2c** intermediate would revert to **2o-AP(S$_0$)** thermally rather than yielding **2c$^+$**. It is expected that increasing the dehydrogenate capability of **2c** by incorporating electron-donating groups would promote the **2c** → **2c$^+$** efficiency. Third, according to the potential energy profiles, the relaxation from **1o-AP-FC(S$_1$)** to **1o-AP-CI** is barrierless, thus inhibiting ISC to triplet states. However, on the S$_1$ surface of **2o-AP**, the minimum energy intermediate **2o(S$_1$)** has a slightly lower energy than **2o-CI(S$_1$)**, so the process of approaching the CI region or the ring-
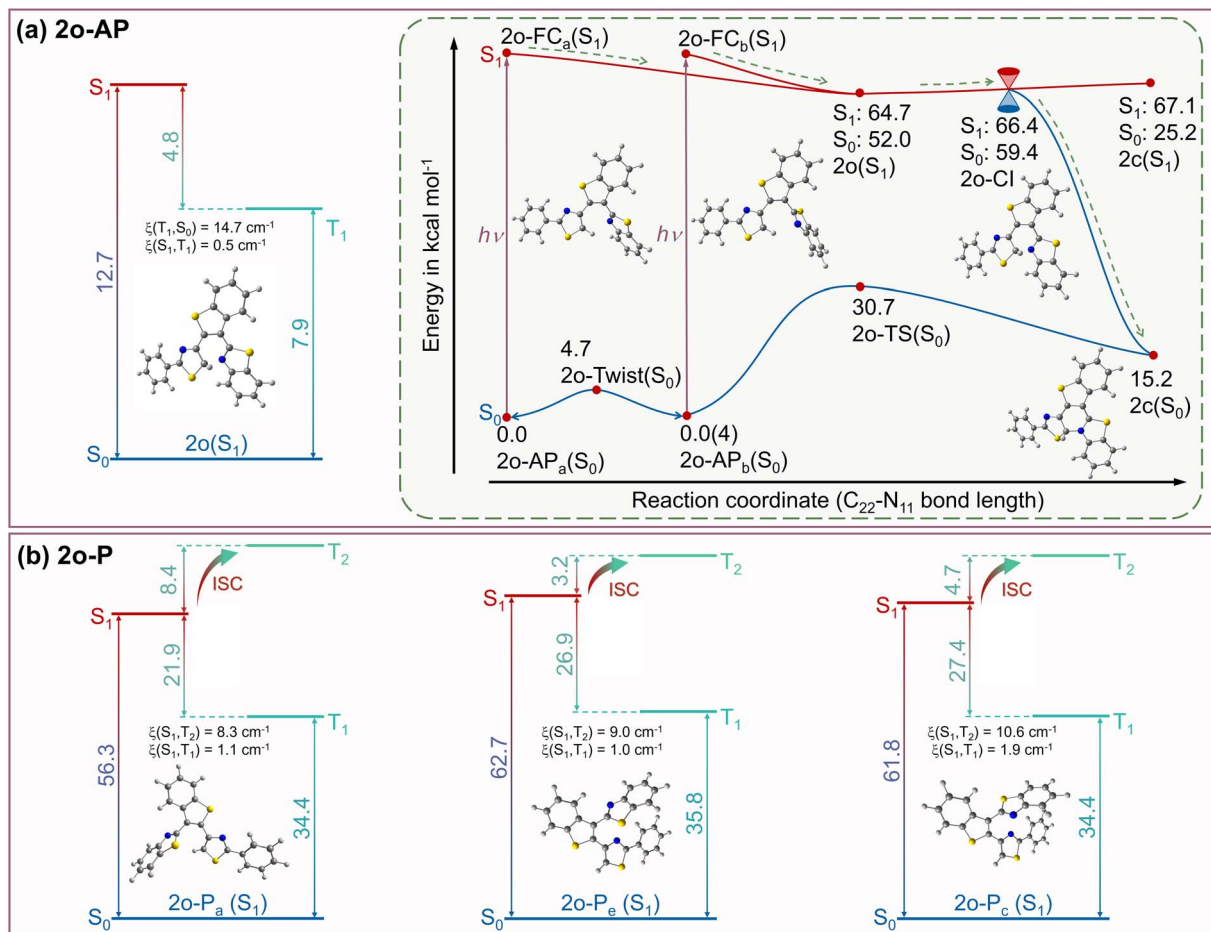
© 2024 The Author(s). Published by the Royal Society of Chemistry

Fig. 5 The calculated singlet and triplet state energy level diagram for (a) **2o-AP** and (b) **2o-P**. Inset: PEC of **2o-AP**: blue line for the S_0 state, red line for the S_1 state, and the green dotted line represents the path of the photochemical reaction (energy in kcal mol^{-1}) (the ground state energy of **2o-AP$_a$(S$_0$)** is used as zero for obtaining relative energies). [(TD)M062X/6-311G**/SMD (THF)].

closed conformation along the reaction pathway is endo-thermic. This leads to a decrease in the IC quantum yield because it cannot compete with the energetically favored ISC pathway. Fourth, the N and S-containing heterocycles usually give rise to enhanced SOC strength and are beneficial for promoted ISC efficiency.[43–46] As a fact, the SOCME for the ISC channel of PHGs is larger than that of PAGs. Additionally, the extended conjugating system lowers the energy of triplet states and offers more possible ISC channels for low-lying singlet states. Since the triplet pathway is a competing side-reaction with respect to the cyclization pathway in the singlet states, reducing the ISC efficiency is a feasible way to improve the release quantum yield of PHGs.

Experimental

Synthesis of compounds

1o and **2o** were prepared following reported methods.[14,42]

1o. ^{1}H NMR (600 MHz, CDCl$_3$): δ 1.52, 2.35 (s, 3H, conformation isomer), 1.64, 2.56 (s, 3H, conformation isomer) 7.10–7.47 (m, 10H) 7.54–7.67 (m, 2H), 7.94–8.10 (m, 3H).

2o. ^{1}H NMR (600 MHz, CDCl$_3$): δ 8.23 (dt, 1H), 7.98 (ddd, 1H), 7.95–7.88 (m, 4H), 7.67–7.56 (m, 1H), 7.53–7.47 (m, 1H), 7.46–7.38 (m, 5H), 7.35 (s, 1H).

The ^{1}H NMR results are shown in Fig. S1 and S2,† respectively.

Photolysis experiments

The photolysis experiment was conducted in a Rayonet RPR 100 containing 16 lamps (266 nm). Cooling was achieved with an internal cold finger. The UV-vis spectra were used to monitor the photolysis process of **1o**.

fs-TA experiment

A femtosecond regenerative amplified Ti:sapphire laser system was applied to carry out the fs-TA experiments. A white continuum light (330–800 nm) was selected as the probe pulse, which was generated in a CaF$_2$ crystal by about 5% of the amplified 800 nm output obtained from the laser system. The probe pulse was divided into two beams; one beam would pass through the sample solution sealed in a 2 mm path-length cuvette, and the other was used as a reference to monitor the

stability of the probe pulse. A 266 nm laser beam was employed to excite **1o**, and a 355 nm laser beam was employed to excite **2o**.

ns-TA experiment

ns-TA experiments were performed on a laser flash spectrometer (LP-980, Edinburgh Instruments). A 266 nm pulse from the fourth harmonic output and a 355 nm pulse from the third harmonic output of the Nd:YAG laser were used as the pump beam, and a 150-W xenon lamp was used as the probe light source. Sample solutions of **1o** and **2o** with absorbance of 0.6 at 266 nm and 355 nm respectively were prepared and placed in a 1 cm quartz cuvette.

DFT calculations

The optimized geometries for the ground state intermediates associated with the reaction pathways of **1o** and **2o** were determined by DFT calculations using the M062X functional with the 6-311G** basis set. The excited state intermediates' geometries and UV-vis spectra were computed by TD-DFT/M062X/6-311G** calculations. For all optimized geometries, vibrational frequency calculations were carried out to verify whether is a minimum (zero imaginary frequency) or transition state (TS) (only one imaginary frequency). Additionally, the transition states (TS) were also confirmed through intrinsic reaction coordinate (IRC) calculations. The PECs along the corresponding reaction coordinate on the S_1 or S_0 state were recorded by a relaxed scan approach, and geometry optimization was performed at each step with the scanned variable (internal coordinate) maintained constant. All the theoretical calculations mentioned above were performed using the Gaussian 16 program.[47] The spin–orbit coupling matrix elements (SOCME) were calculated at the TD-DFT/M062X/6-311G** level of theory with spin–orbit mean-field (SOMF) methods employing the ORCA 5.0.3 program,[48] and the solvent effects of ACN ($\varepsilon = 37.5$) and THF ($\varepsilon = 7.52$) were accounted for by the SMD model.[49] The Cartesian coordinates, energies and free energies for all intermediates in the S_0, S_1, and T_1 states involved in the reaction paths are listed in the ESI†. Multiwfn software was applied to analyze the excitation characteristics and atomic charge distributions.[50]

Conclusions

In order to help the rational design of PHGs with improved quantum yield, the photochemical reaction mechanisms of **1o** and **2o** as PAGs and PHGs models are extensively investigated by utilizing time-resolved spectroscopy and DFT/TD-DFT calculations. It is unravelled that **1o** and **2o** follow different reaction pathways upon photoexcitation. The spontaneous cyclization process of **1o** takes place immediately after pumped to the singlet excited state, generating the semi-closing intermediate (**1c**) which lies in the vicinity of the CI region. After decay to the S_0 state, the release of the triflate anion from **1o** follows a synergistic pattern, that is, the ring-closing and de-acidification occur simultaneously. The entire photoinduced reaction process of **1o** completes within a few ps. On the other hand, the

ring closure and hydride release of **2o** occur stepwise in the presence of a hydride receptor. Being excited to the FC region of the singlet excited state, **2o** first relaxes to the S_1 minimum, which decays to S_0 by climbing up the barrier approaching the CI region and forming the closed-form intermediate **2c**. Generation of **2c$^+$** can only take place with the aid of a hydride acceptor. Based on the detailed reaction mechanisms, several design principles for efficient PHGs are proposed. The current work unveils the structure–reactivity relationship for rational design of novel versatile photoacid and photohydride generators, as well as presenting general suggestions for developing advanced PHG based optical materials.

Data availability

The data that support the findings of this study are available in the ESI.†

Author contributions

Yifan Su: investigation, methodology, data curation, visualization, software and writing – original draft. Dexin Zheng and Lingfeng Ge: investigation, methodology and writing – review & editing. Le Yu: theoretical calculations, supervision and writing – review & editing. Jiani Ma: resources, validation, investigation, data curation, supervision and writing – review & editing. David Lee Phillips and Yu Fang: investigation, supervision and writing – review & editing.

Conflicts of interest

There are no conflicts to declare.

Acknowledgements

References

1 M. J. Hansen, W. A. Velema, M. M. Lerch, W. Szymanski and B. L. Feringa, *Chem. Soc. Rev.*, 2015, **44**, 3358–3377.
2 M. Klausen and M. Blanchard-Desce, *J. Photochem. Photobiol., C*, 2021, **48**, 100423.
3 G. C. R. Ellis-Davies, *Angew. Chem., Int. Ed.*, 2023, **62**, e202206083.
4 C. C. Romão, W. A. Blättler, J. D. Seixas and G. J. L. Bernardes, *Chem. Soc. Rev.*, 2012, **41**, 3571–3583.
5 M. Klimezak, J. Chaud, A. Brion, F. Bolze, B. Frisch, B. Heurtault, A. Kichler and A. Specht, *Adv. Healthcare Mater.*, 2024, **13**, 2400354.

6 C. A. Hammer, K. Falahati, A. Jakob, R. Klimek, I. Burghardt, A. Heckel and J. Wachtveitl, *J. Phys. Chem. Lett.*, 2018, **9**, 1448–1453.

7 Y. A. Jézéquel, F. Svěrák, A. Ramundo, V. Orel, M. Martínek and P. Klán, *J. Org. Chem.*, 2024, **89**, 4888–4903.

8 A. Sikder, M. Banerjee, T. Singha, S. Mondal, P. K. Datta, A. Anoop and N. D. P. Singh, *Org. Lett.*, 2020, **22**, 6998–7002.

9 S. Banala, M. C. Arvin, N. M. Bannon, X.-T. Jin, J. J. Macklin, Y. Wang, C. Peng, G. Zhao, J. J. Marshall, K. R. Gee, D. L. Wokosin, V. J. Kim, J. M. McIntosh, A. Contractor, H. A. Lester, Y. Kozorovitskiy, R. M. Drenan and L. D. Lavis, *Nat. Methods*, 2018, **15**, 347–350.

10 C. C. Warford, C.-J. Carling and N. R. Branda, *Chem. Commun.*, 2015, **51**, 7039–7042.

11 C. Berton, D. M. Busiello, S. Zamuner, E. Solari, R. Scopelliti, F. Fadaei-Tirani, K. Severin and C. Pezzato, *Chem. Sci.*, 2020, **11**, 8457–8468.

12 Y. Liao, *Acc. Chem. Res.*, 2017, **50**, 1956–1964.

13 Y. Cheng, X. Ma, J. Zhai and X. Xie, *Chem. Commun.*, 2023, **59**, 1805–1808.

14 R. Mizutsu, R. Asato, C. J. Martin, M. Yamada, Y. Nishikawa, S. Katao, M. Yamada, T. Nakashima and T. Kawai, *J. Am. Chem. Soc.*, 2019, **141**, 20043–20047.

15 R. Weinstain, T. Slanina, D. Kand and P. Klán, *Chem. Rev.*, 2020, **120**, 13135–13272.

16 T. Sun, L. Kang, H. Zhao, Y. Zhao and Y. Gu, *Adv. Sci.*, 2024, **11**, 2302875.

17 N. Zivic, P. K. Kuroishi, F. Dumur, D. Gigmes, A. P. Dove and H. Sardon, *Angew. Chem., Int. Ed.*, 2019, **58**, 10410–10422.

18 K. Sambath, Z. Wan, Q. Wang, H. Chen and Y. Zhang, *Org. Lett.*, 2020, **22**, 1208–1212.

19 L. D. Terlizzi, A. Martinelli, D. Merli, S. Protti and M. Fagnoni, *J. Org. Chem.*, 2023, **88**, 6313–6321.

20 Z. Shi, P. Peng, D. Strohecker and Y. Liao, *J. Am. Chem. Soc.*, 2011, **133**, 14699–14703.

21 A. N. Komogortsev, C. V. Milyutin, B. V. Lichitsky and V. G. Melekhina, *Tetrahedron*, 2022, **114**, 132780.

22 C. J. Martin, J. P. Calupitan, M. Minamide, R. Asato, Y. Goto, G. Rapenne, T. Nakashima and T. Kawai, *J. Photochem. Photobiol., A*, 2020, **397**, 112594.

23 A. McSkimming and S. B. Colbran, *Chem. Soc. Rev.*, 2013, **42**, 5439–5488.

24 X. Yang, J. Walpita, D. Zhou, H. L. Luk, S. Vyas, R. S. Khnayzer, S. C. Tiwari, K. Diri, C. M. Hadad, F. N. Castellano, A. I. Krylov and K. D. Glusac, *J. Phys. Chem. B*, 2013, **117**, 15290–15296.

25 A. G. Lvov, E. K. Kouame and M. M. Khusniyarov, *Chem.–Eur. J.*, 2023, **29**, e202301480.

26 J. Volarić, W. Szymanski, N. A. Simeth and B. L. Feringa, *Chem. Soc. Rev.*, 2021, **50**, 12377–12449.

27 O. Galangau, S. Delbaere, N. Ratel-Ramond, G. Rapenne, R. Li, J. P. D. C. Calupitan, T. Nakashima and T. Kawai, *J. Org. Chem.*, 2016, **81**, 11282–11290.

28 A. G. Lvov, V. Z. Shirinian, V. V. Kachala, A. M. Kavun, I. V. Zavarzin and M. M. Krayushkin, *Org. Lett.*, 2014, **16**, 4532–4535.

29 A. V. Zakharov, E. B. Gaeva, A. G. Lvov, A. V. Metelitsa and V. Z. Shirinian, *J. Org. Chem.*, 2017, **82**, 8651–8661.

30 R. Murata, T. Yago and M. Wakasa, *J. Phys. Chem. A*, 2015, **119**, 11138–11145.

31 K. Tani, Y. Ishibashi, H. Miyasaka, S. Kobatake and M. Irie, *J. Phys. Chem. C*, 2008, **112**, 11150–11157.

32 M. T. Indelli, S. Carli, M. Ghirotti, C. Chiorboli, M. Ravaglia, M. Garavelli and F. Scandola, *J. Am. Chem. Soc.*, 2008, **130**, 7286–7299.

33 S. Fredrich, T. Morack, M. Sliwa and S. Hecht, *Chem.–Eur. J.*, 2020, **26**, 7672–7677.

34 A. V. Yadykov, A. G. Lvov, M. M. Krayushkin, A. V. Zakharov and V. Z. Shirinian, *J. Org. Chem.*, 2021, **86**, 10023–10031.

35 P. Ravat, T. Šolomek, D. Häussinger, O. Blacque and M. Juríček, *J. Am. Chem. Soc.*, 2018, **140**, 10839–10847.

36 Y. Nakakuki, T. Hirose, H. Sotome, M. Gao, D. Shimizu, R. Li, J. Hasegawa, H. Miyasaka and K. Matsuda, *Nat. Commun.*, 2022, **13**, 1475.

37 H. Hamamoto, D. Shimizu and K. Matsuda, *Chem.–Eur. J.*, 2024, **30**, e202401353.

38 A. G. Lvov, V. Z. Shirinian, A. V. Zakharov, M. M. Krayushkin, V. V. Kachala and I. V. Zavarzin, *J. Org. Chem.*, 2015, **80**, 11491–11500.

39 A. V. Zakharov, A. V. Yadykov, E. B. Gaeva, A. V. Metelitsa and V. Z. Shirinian, *J. Org. Chem.*, 2021, **86**, 16806–16814.

40 T. Nakashima, K. Tsuchie, R. Kanazawa, R. Li, S. Iijima, O. Galangau, H. Nakagawa, K. Mutoh, Y. Kobayashi, J. Abe and T. Kawai, *J. Am. Chem. Soc.*, 2015, **137**, 7023–7026.

41 R. Li, T. Nakashima and T. Kawai, *Chem. Commun.*, 2017, **53**, 4339–4341.

42 C. J. Martin, M. Minamide, J. P. D. C. Calupitan, R. Asato, J. Kuno, T. Nakashima, G. Rapenne and T. Kawai, *J. Org. Chem.*, 2018, **83**, 13700–13706.

43 T. Yang, Y. Li, Z. Zhao and W. Z. Yuan, *Sci. China Chem.*, 2023, **66**, 367–387.

44 N. Aizawa, A. Matsumoto and T. Yasuda, *Sci. Adv.*, 2021, **7**, eabe5769.

45 L. Ma, Y. Liu, H. Tian and X. Ma, *JACS Au*, 2023, **3**, 1835–1842.

46 Y. Tu, J. Liu, H. Zhang, Q. Peng, J. W. Y. Lam and B. Z. Tang, *Angew. Chem., Int. Ed.*, 2019, **58**, 14911–14914.

47 M. J. Frisch, G. W. Trucks, H. B. Schlegel, G. E. Scuseria, M. A. Robb, J. R. Cheeseman, G. Scalmani, V. Barone, G. A. Petersson, H. Nakatsuji, X. Li, M. Caricato, A. V. Marenich, J. Bloino, B. G. Janesko, R. Gomperts, B. Mennucci, H. P. Hratchian, J. V. Ortiz, A. F. Izmaylov, J. L. Sonnenberg, D. Williams-Young, F. Ding, F. Lipparini, F. Egidi, J. Goings, B. Peng, A. Petrone, T. Henderson, D. Ranasinghe, V. G. Zakrzewski, J. Gao, N. Rega, G. Zheng, W. Liang, M. Hada, M. Ehara, K. Toyota, R. Fukuda, J. Hasegawa, M. Ishida, T. Nakajima, Y. Honda, O. Kitao, H. Nakai, T. Vreven, K. Throssell, J. A. Montgomery Jr, J. E. Peralta, F. Ogliaro, M. J. Bearpark, J. J. Heyd, E. N. Brothers, K. N. Kudin, V. N. Staroverov, T. A. Keith, R. Kobayashi, J. Normand, K. Raghavachari, A. P. Rendell, J. C. Burant, S. S. Iyengar, J. Tomasi, M. Cossi, J. M. Millam, M. Klene, C. Adamo,

R. Cammi, J. W. Ochterski, R. L. Martin, K. Morokuma, O. Farkas, J. B. Foresman and D. J. Fox, *Gaussian 16, rev. A.03*, Gaussian, Inc., Wallingford, CT, 2016.

48 F. Neese, Software update: The ORCA program system-Version 5.0, *Wiley Interdiscip. Rev.: Comput. Mol. Sci.*, 2022, **12**, e1606.

49 A. V. Marenich, C. J. Cramer and D. G. Truhlar, *J. Phys. Chem. B*, 2009, **113**, 6378–6396.

50 T. Lu and F. Chen, *J. Comput. Chem.*, 2012, **33**, 580–592.